GEOPHYSICS, VOL. 87, NO. 1 (JANUARY-FEBRUARY 2022); P. R111–R122, 13 FIGS.
10.1190/GEO2021-0306.1

Check for updates

Downloaded 03/10/22 to 138.67.12.93. Redistribution subject to SEG license or copyright; see Terms of Use at http://library.seg.org/page/policies/terms
DOI:10.1190/geo2021-0306.1

Source-independent time-lapse full-waveform inversion for anisotropic media

Yanhua Liu[1] and Ilya Tsvankin[1]

ABSTRACT

Time-lapse full-waveform inversion can provide high-resolution information about changes in the reservoir properties during hydrocarbon production and CO_2 injection. However, the accuracy of the estimated source wavelet, which is critically important for time-lapse FWI, is often insufficient for field-data applications. The so-called "source-independent" FWI is designed to reduce the influence of the source wavelet on the inversion results. We incorporate the convolution-based source-independent technique into a time-lapse FWI algorithm for VTI (transversely isotropic with a vertical symmetry axis) media. The gradient of the modified FWI objective function is obtained from the adjoint-state method. The algorithm is tested on a model with a graben structure and the modified VTI Marmousi model using three time-lapse strategies (the parallel-difference, sequential-difference, and double-difference methods). The results confirm the ability of the developed methodology to reconstruct the localized time-lapse parameter variations even for a strongly distorted source wavelet. The algorithm remains robust in the presence of moderate noise in the input data but the accuracy of the estimated time-lapse changes depends on the model complexity.

INTRODUCTION

Because seismic signatures are sensitive to the changes (e.g., in pressure and saturation) inside the reservoir, seismic time-lapse monitoring has been widely used for optimizing hydrocarbon production and CO_2 injection (Lumley, 2010; Smith and Tsvankin, 2013; Pevzner et al., 2017). Full-waveform inversion (FWI) is an established tool for high-resolution velocity analysis and has been applied to reservoir characterization (Vigh et al., 2014; Asnaashari et al., 2015; Singh et al., 2018; Zhang and Alkhalifah, 2020; Li et al., 2021). FWI iteratively updates the medium parameters by minimizing the misfit between the observed and simulated seismic data.

Unlike conventional time-lapse methods, FWI operates with both the phase and amplitude of seismic waves, which can potentially increase the resolution of the inverted time-lapse parameter variations. However, FWI requires an accurate estimate of the source wavelet. Errors in the source signature (e.g., in its shape, frequency, or amplitude) can hinder matching of the simulated and observed data and distort the inversion results (Song et al., 1995; Pratt, 1999; Warner et al., 2013; Luo et al., 2014; Yuan et al., 2014). This issue is particularly important for time-lapse FWI because of the commonly observed nonrepeatability of the source signature between the baseline and monitor surveys. In particular, seasonal changes in the near surface may produce dramatic changes in the source signal (Jervis et al., 2018).

One way to reconstruct the source wavelet in FWI is to iteratively estimate it during the inversion along with the medium parameters (Song et al., 1995; Pratt, 1999; Xu et al., 2006). However, this method incurs a substantial computational cost, introduces additional trade-offs, and requires an accurate initial approximation for the source wavelet (Xu et al., 2006).

A more practical alternative is the so-called "source-independent" method designed to reduce the influence of the source signature on the inversion results. Deconvolution-based trace normalization can be employed in the frequency domain to remove information about the source wavelet from both the recorded and modeled data (Lee and Kim, 2003; Zhou and Greenhalgh, 2003; Seo et al., 2005; Choi and Min, 2012). Choi et al. (2005) propose to define the objective function in the frequency domain by multiplying the data with the corresponding reference trace. However, the resolution achieved by this deconvolution-based method strongly depends on the signal-to-noise ratio.

Choi and Alkhalifah (2011) define the convolution-based source-independent FWI objective function in the time domain. The first step is to choose a reference trace from both the observed and

Manuscript received by the Editor 21 May 2021; revised manuscript received 1 September 2021; published ahead of production 22 October 2021; published online 21 December 2021.
[1]Colorado School of Mines, Center for Wave Phenomena, Golden, Colorado 80401, USA. E-mail: liuyanhua@mymail.mines.edu (corresponding author); ilya@mines.edu.
© 2022 Society of Exploration Geophysicists. All rights reserved.

Downloaded 03/10/22 to 138.67.12.93. Redistribution subject to SEG license or copyright; see Terms of Use at http://library.seg.org/page/policies/terms
DOI:10.1190/geo2021-0306.1

simulated data sets. Then the simulated data are convolved with the reference trace from the observed data, and the observed data are convolved with the reference trace from the simulated data. The modified FWI objective function is designed to minimize the difference between these two convolved data sets. One issue with this approach is that the convolution and cross-correlation operations tend to generate additional noise, which can be suppressed by applying a time window to the reference traces beforehand (Zhang et al., 2016). Wang and Alkhalifah (2018) employ the source-independent objective function to estimate the location and excitation times of microseismic sources. Bai and Tsvankin (2019) extend the time-domain source-independent waveform inversion to attenuation estimation using reflection or transmission data from VTI media. Wang et al. (2020) use the source-independent FWI to mitigate cycle skipping caused by the unknown source signature of passive events and apply their algorithm to a field data set.

Liu and Tsvankin (2021) develop a time-lapse FWI algorithm for VTI media and test it on synthetic data using three common time-lapse strategies (Asnaashari et al., 2015): the parallel-difference (Plessix et al., 2010), sequential-difference, and double-difference techniques (Watanabe et al., 2004; Denli and Huang, 2009). The parallel-difference method uses the same initial model for the baseline and monitor FWI, whereas the sequential-difference method inverts the baseline data to build the initial model for the monitor inversion. The double-difference technique directly estimates the time-lapse parameter variations from the difference between the monitor and baseline data sets.

As mentioned previously, time-lapse FWI is particularly sensitive to the accuracy of the source wavelet. Note that even moderate wavelet-related distortions in the inversion of the baseline and monitor data can lead to large percentage errors in the estimated time-lapse parameter variations. Most existing time-lapse processing algorithms either assume the source wavelet to be known or iteratively estimate it during the inversion.

Here, we extend the convolution-based source-independent method to time-lapse FWI of reflection data from VTI media. This extension involves adaptation of the source-independent technique for different time-lapse strategies, in particular for the double-difference method.

We begin by discussing the methodology of the source-independent FWI technique and outline its application to time-lapse seismic. Analysis of the corresponding objective function is followed by a brief review of the three previously mentioned time-lapse strategies. The derivation of the inversion gradients in terms of the VTI parameters is given in the appendix. The proposed algorithm is applied to the reconstruction of the time-lapse parameter variations in a VTI graben model and in a modified version of the VTI Marmousi model. The inversion results are used to evaluate the robustness of the source-independent algorithm implemented with different time-lapse strategies. We also discuss the influence of the reference trace, time window, and noise on the inverted time-lapse variations.

METHODOLOGY OF SOURCE-INDEPENDENT TIME-LAPSE FWI

FWI of time-lapse seismic data generally involves the inversion of baseline and monitor surveys. The baseline survey is often acquired before hydrocarbon production or CO_2 injection, and the monitor survey during or after production/injection. Typically, FWI is first applied to the baseline data to obtain the baseline model. Then the monitor survey is processed using different approaches according to the chosen time-lapse strategy. The subtraction of the inverted baseline model from the monitor model yields the time-lapse parameter variations.

Conventional FWI algorithms use the L_2-norm objective function (e.g., Tarantola, 1984) for the inversion of the baseline (subscript b) data:

$$S_{\mathrm{b}}(\mathbf{m}_{\mathrm{b}}) = \frac{1}{2}\|[\mathbf{d}_{\mathrm{b}}^{\mathrm{sim}}(\mathbf{m}_{\mathrm{b}}) - \mathbf{d}_{\mathrm{b}}^{\mathrm{obs}}]\|^2 = \frac{1}{2}\|[\mathbf{G}^{\mathrm{sim}} * \mathbf{s}^{\mathrm{sim}} - \mathbf{G}^{\mathrm{obs}} * \mathbf{s}^{\mathrm{obs}}]\|^2, \tag{1}$$

where $\mathbf{d}_{\mathrm{b}}^{\mathrm{sim}}$ is the data simulated for the baseline model $\mathbf{m}_{\mathrm{b}}$, $\mathbf{d}_{\mathrm{b}}^{\mathrm{obs}}$ is the observed baseline data, the symbol "*" denotes convolution, $\mathbf{G}^{\mathrm{sim}}$ and $\mathbf{G}^{\mathrm{obs}}$ are the simulated and actual Green's functions, respectively, and $\mathbf{s}^{\mathrm{sim}}$ and $\mathbf{s}^{\mathrm{obs}}$ are the simulated and actual source wavelets.

Source-independent methodology

To reduce the influence of the source wavelet, Choi and Alkhalifah (2011) and Zhang et al. (2016) propose the following convolution-based source-independent objective function in the time domain:

$$\begin{aligned} S_{\mathrm{b}}(\mathbf{m}_{\mathrm{b}}) &= \frac{1}{2}\|[\mathbf{d}_{\mathrm{b}}^{\mathrm{sim}}(\mathbf{m}_{\mathrm{b}}) * (W\mathbf{d}_{\mathrm{ref}}^{\mathrm{obs}}) - \mathbf{d}_{\mathrm{b}}^{\mathrm{obs}} * (W\mathbf{d}_{\mathrm{ref}}^{\mathrm{sim}})]\|^2 \\ &= \frac{1}{2}\|[\mathbf{G}^{\mathrm{sim}} * \mathbf{s}^{\mathrm{sim}} * W\mathbf{G}_{\mathrm{ref}}^{\mathrm{obs}} * \mathbf{s}^{\mathrm{obs}} - \mathbf{G}^{\mathrm{obs}} * \mathbf{s}^{\mathrm{obs}} * W\mathbf{G}_{\mathrm{ref}}^{\mathrm{sim}} * \mathbf{s}^{\mathrm{sim}}]\|^2 \\ &= \frac{1}{2}\|[\tilde{\mathbf{G}}^{\mathrm{s}} * \tilde{\mathbf{s}}^{\mathrm{c}} - \tilde{\mathbf{G}}^{\mathrm{o}} * \tilde{\mathbf{s}}^{\mathrm{c}}]\|^2, \end{aligned} \tag{2}$$

where $W = W(t)$ is the chosen time window, and $\mathbf{d}_{\mathrm{ref}}$ denotes the reference trace. $\mathbf{G}_{\mathrm{ref}}^{\mathrm{obs}}$ and $\mathbf{G}_{\mathrm{ref}}^{\mathrm{sim}}$ are the Green's functions for the reference traces, $\tilde{\mathbf{G}}^{\mathrm{s}}$ and $\tilde{\mathbf{G}}^{\mathrm{o}}$ are the Green's functions for the new convolution-based simulated and observed data, and $\tilde{\mathbf{s}}^{\mathrm{c}}$ is the new source wavelet. The expressions for $W(t)$, $\tilde{\mathbf{G}}^{\mathrm{s}}$, $\tilde{\mathbf{G}}^{\mathrm{o}}$, and $\tilde{\mathbf{s}}^{\mathrm{c}}$ are:

$$\text{Time window}: W(t) = \begin{cases} 1 & t_l \le t \le t_h; \\ 0 & \text{otherwise.} \end{cases} \tag{3}$$

$$\text{New Green's functions}: \begin{cases} \tilde{\mathbf{G}}^{\mathrm{s}} = \mathbf{G}^{\mathrm{sim}} * W\mathbf{G}_{\mathrm{ref}}^{\mathrm{obs}}; \\ \tilde{\mathbf{G}}^{\mathrm{o}} = \mathbf{G}^{\mathrm{obs}} * W\mathbf{G}_{\mathrm{ref}}^{\mathrm{sim}}. \end{cases} \tag{4}$$

$$\text{New source wavelet}: \tilde{\mathbf{s}}^{\mathrm{c}} = \mathbf{s}^{\mathrm{sim}} * \mathbf{s}^{\mathrm{obs}}. \tag{5}$$

Here, t_l and t_h are the boundaries of the time window applied to the reference trace.

The new simulated and observed data in equation 2 could be expressed as the convolutions of the new Green's functions ($\tilde{\mathbf{G}}^{\mathrm{s}}$ and $\tilde{\mathbf{G}}^{\mathrm{o}}$) and the source wavelet ($\tilde{\mathbf{s}}^{\mathrm{c}}$). Because the wavelet $\tilde{\mathbf{s}}^{\mathrm{c}}$ is the same for the simulated and observed data, the deviation of the estimated source signature from the actual wavelet is theoretically eliminated from the modified objective function.

Downloaded 03/10/22 to 138.67.12.93. Redistribution subject to SEG license or copyright; see Terms of Use at http://library.seg.org/page/policies/terms
DOI:10.1190/geo2021-0306.1

The time window $W(t)$ is used to mitigate the artifacts caused by the convolution and cross-correlation operations. To save computing time and ensure efficient noise suppression, the time window should be as short as possible but has to contain sufficient information about the source wavelet. Zhang et al. (2016) suggest that the lower cut-off time (t_l) should be before the first arrival, and the window should contain at least one full waveform, such as the P-wave direct arrival. Here, we define the time window using the Butterworth filter:

$$W(t) = \frac{1}{1 + \left(\frac{t - t_l}{t_h}\right)^{2n}} = \frac{1}{1 + \left(\frac{t - t_l}{t_h}\right)^{30}}, \tag{6}$$

where n is the order of the filter ($n = 15$ in our examples).

Implementation of time-lapse FWI

We parameterize VTI media by the velocities V_{P0} (P-wave vertical velocity), V_{S0} (S-wave vertical velocity), $V_{hor,P}$ (P-wave horizontal velocity), $V_{nmo,P}$ (P-wave normal-moveout velocity from a horizontal reflector), and density ρ (Tsvankin, 2012; Alkhalifah and Plessix, 2014; Kamath and Tsvankin, 2016; Zhang et al., 2018; Singh et al., 2020). Multicomponent data are simulated by solving the 2D wave equation for elastic, arbitrarily heterogeneous VTI media with a fourth-order finite-difference algorithm (Singh et al., 2020). All five VTI parameters are updated simultaneously using the gradients derived in Appendix A.

The time-lapse strategies employed here use the same objective function for the baseline inversion but differ in handling the monitor survey (or the time-lapse data difference). In the parallel-difference approach (Plessix et al., 2010), the baseline and monitor inversions are performed independently but with the same initial model. The time-lapse model produced by this method can remain sufficiently accurate when the errors in the inverted baseline and monitor models are similar. The sequential-difference strategy (Asnaashari et al., 2012) uses the inversion of the baseline data to build the initial model for FWI of the monitor survey. This facilitates the convergence of the monitor inversion due to the similarity between the baseline and monitor surveys.

In the double-difference method (Denli and Huang, 2009; Waldhauser and Ellsworth, 2020), the monitor inversion operates directly on the difference between the monitor and baseline data ($\mathbf{d}_m^{obs} - \mathbf{d}_b^{obs}$). The monitor model is obtained by minimizing the difference $\Delta\mathbf{d}$ between the simulated monitor data $\mathbf{d}_m^{sim}$ and the "composite" data $\mathbf{d}_{com}$, starting from the inverted baseline model:

$$\Delta\mathbf{d} = (\mathbf{d}_m^{obs} - \mathbf{d}_b^{obs}) - (\mathbf{d}_m^{sim} - \mathbf{d}_b^{sim}) = \mathbf{d}_{com} - \mathbf{d}_m^{sim}, \tag{7}$$

$$\mathbf{d}_{com} = \mathbf{d}_m^{obs} - \mathbf{d}_b^{obs} + \mathbf{d}_b^{sim}, \tag{8}$$

where $\mathbf{d}_b^{sim}$ is the data simulated for the inverted baseline model.

Because the double-difference method operates on the data difference, the geometries of the baseline and monitor surveys should be similar and the amplitude of the data difference should be above the noise level.

SYNTHETIC EXAMPLES

The developed source-independent time-lapse FWI algorithm is tested on a VTI graben model and the modified VTI Marmousi model. The synthetic data for both models are generated with the Ricker wavelet (Figure 1a). The source-independent algorithm is applied for two distorted wavelets (Figure 1b and 1c) used in the inversion. FWI is implemented for multicomponent surface data (vertical and horizontal velocities) using the multiscale approach with four frequency bands starting at 2 Hz (Singh et al., 2020).

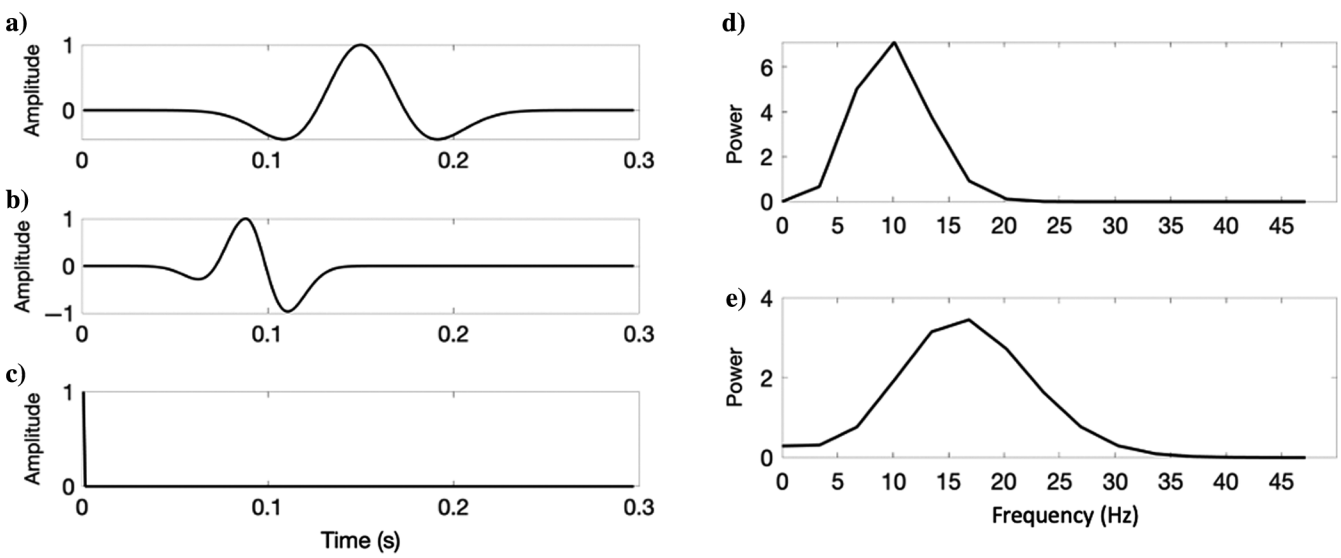

Figure 1. Source wavelets used in the synthetic examples: (a) the Ricker wavelet with a central frequency of 10 Hz (actual wavelet), (b) the distorted "Ricker" wavelet with a central frequency of 17 Hz (Wavelet 1), and (c) the spike (Wavelet 2). The frequency spectra of (d) the actual wavelet (see plot [a]) and (e) Wavelet 1 (see plot [b]).

Downloaded 03/10/22 to 138.67.12.93. Redistribution subject to SEG license or copyright; see Terms of Use at http://library.seg.org/page/policies/terms
DOI:10.1190/geo2021-0306.1

VTI graben model

The elastic wavefield is excited by 58 shots (point explosions) placed with a constant increment (80 m) along a horizontal line at a depth of 40 m (Figure 2a). We employ 400 receivers evenly distributed with an increment of 10 m along the horizontal line at a depth of 100 m. The medium parameters for the monitor survey (Liu and Tsvankin, 2021) are obtained by reducing the baseline vertical velocities V_{P0}, V_{S0}, and density ρ in the target area (i.e., in the dipping layer segments) by approximately 10% (Figure 2). The initial baseline models (Figure 2c, 2f, 2i, 2l, and 2o) are computed by Gaussian smoothing of the actual parameter distributions with a standard deviation of 10.

The benchmark time-lapse results (Figure 3) are obtained by performing FWI with the actual wavelet following the parallel-difference strategy. The time-lapse parameter variations inside the "reservoir" are well estimated and there are no significant artifacts outside the target zone. The artifacts near the boundaries of the graben structure are caused primarily by edge (smoothing) effects (Schmidt, 2005; Zhang and Zhang, 2012) in the L_2-norm objective function.

Next, the conventional FWI algorithm is applied to the baseline data using a distorted source wavelet (Wavelet 1). The incorrect source signature completely corrupts the inversion results, and even the graben structure itself is barely visible (Figure 4). It is clear that conventional FWI will be unable to reconstruct the time-lapse parameter changes for the distorted wavelet.

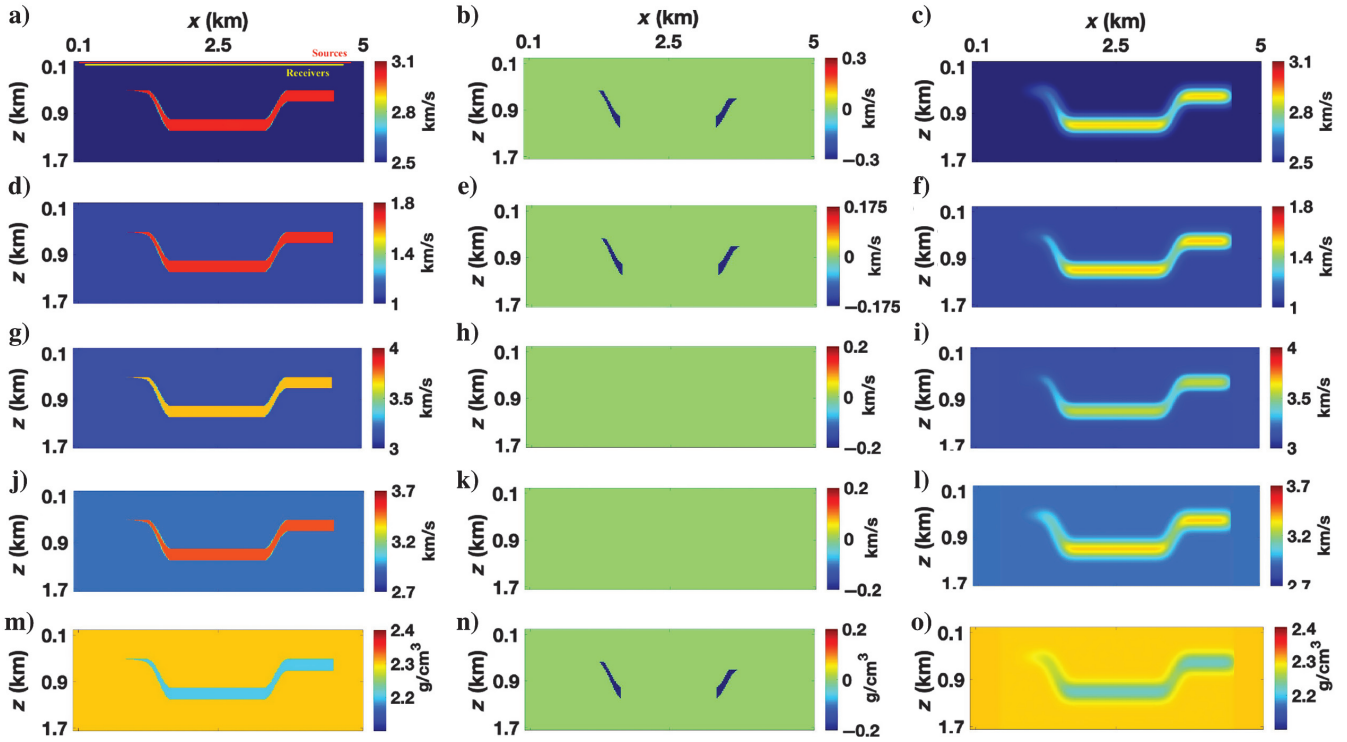

Figure 2. Parameters of the baseline graben model with a grid size of 10 × 10 m: (a) the P-wave vertical velocity (V_{P0}), (d) the S-wave vertical velocity (V_{S0}), (g) the P-wave horizontal velocity ($V_{hor,P}$), (j) the P-wave normal-moveout velocity ($V_{nmo,P}$), and (m) the density (ρ). The actual time-lapse differences for (b) V_{P0}, (e) V_{S0}, (h) $V_{hor,P}$, (k) $V_{nmo,P}$, and (n) ρ. The initial baseline model of: (c) V_{P0}, (f) V_{S0}, (i) $V_{hor,P}$, (l) $V_{nmo,P}$, and (o) ρ.

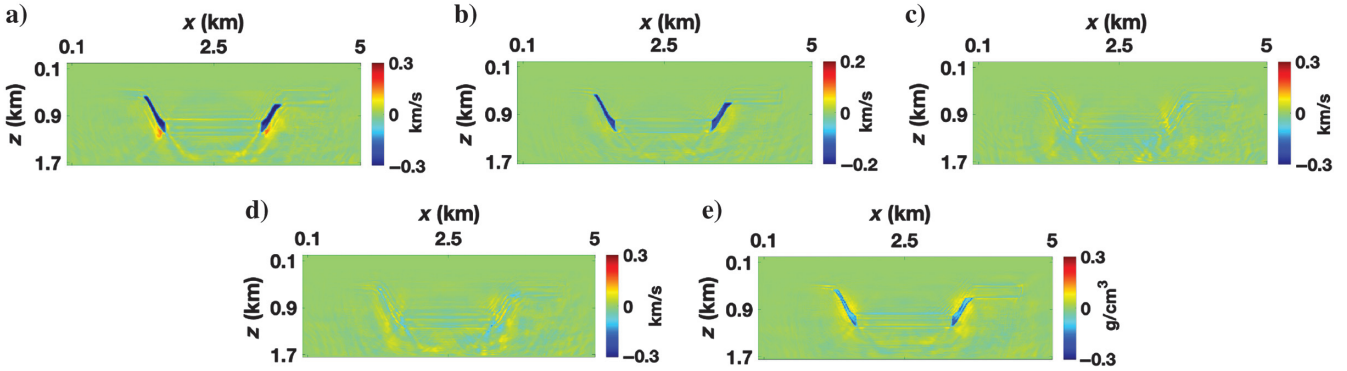

Figure 3. Time-lapse parameter variations obtained by conventional FWI with the actual wavelet using the parallel-difference method (benchmark results): (a) V_{P0}, (b) V_{S0}, (c) $V_{hor,P}$, (d) $V_{nmo,P}$, and (e) ρ.

Downloaded 03/10/22 to 138.67.12.93. Redistribution subject to SEG license or copyright; see Terms of Use at http://library.seg.org/page/policies/terms
DOI:10.1190/geo2021-0306.1

Then we apply the source-independent FWI algorithm using Wavelet 1. After estimating the baseline model, three time-lapse methods are used to reconstruct the parameter variations (note that the P-wave horizontal and NMO velocities are held constant). All five VTI parameters are updated simultaneously during the inversion. The selected reference traces for both the vertical and horizontal particle velocities correspond to the receiver located closest to the source, which ensures high fidelity of the source signal.

Parallel- and sequential-difference methods

The time-lapse changes estimated by the source-independent FWI using the parallel- and sequential-difference strategies are sufficiently close to the benchmark results (Figure 2), although the amplitude of the time-lapse anomalies is slightly underestimated. Also, our method generates some false time-lapse anomalies in the velocities $V_{\mathrm{hor,P}}$ and $V_{\mathrm{nmo,P}}$ because of the parameter trade-offs (Figure 5g, 5h, 5j, and 5k). The performance of the parallel-difference (Figure 5a, 5d, and 5m) and sequential-difference (Figure 5b, 5e, and 5n) methods in reconstructing the time-lapse variations in V_{P0}, V_{S0}, and ρ and suppressing the artifacts is comparable.

The robustness of our algorithm applied with the parallel-difference method is further evaluated in Figure 6 for the spike wavelet that represents an extreme shape distortion. Still, the time-lapse changes of the parameters V_{P0}, V_{S0}, and ρ are reconstructed with sufficient resolution similar to that for Wavelet 1 (Figure 5a, 5d, and 5m). Clearly, our source-independent algorithm can handle even extreme frequency and shape distortions in the source wavelet for high-quality multicomponent data.

Double-difference method

Although the double-difference method does not produce significant false anomalies, the reconstructed temporal variations in V_{P0}, V_{S0}, and ρ have the wrong sign (Figure 5c, 5f, and 5o). In contrast to the other two strategies, this method operates with the "composite" data ($\mathbf{d}_{\mathrm{m}}^{\mathrm{obs}} - \mathbf{d}_{\mathrm{b}}^{\mathrm{obs}} + \mathbf{d}_{\mathrm{b}}^{\mathrm{sim}}$) generated by adding the wavefield simulated for the inverted baseline model to the actual time-lapse data difference (equations 7 and 8). The frequency distortion of Wavelet 1 leads to a phase mismatch between the simulated baseline data $\mathbf{d}_{\mathrm{b}}^{\mathrm{sim}}$ and the observed wavefield. The resulting degradation of the "composite" data set prevents the source-independent algorithm from producing a sufficiently accurate monitor model.

To verify this conjecture, in Figure 7b we use a wavelet which has the shape of Wavelet 1 but the

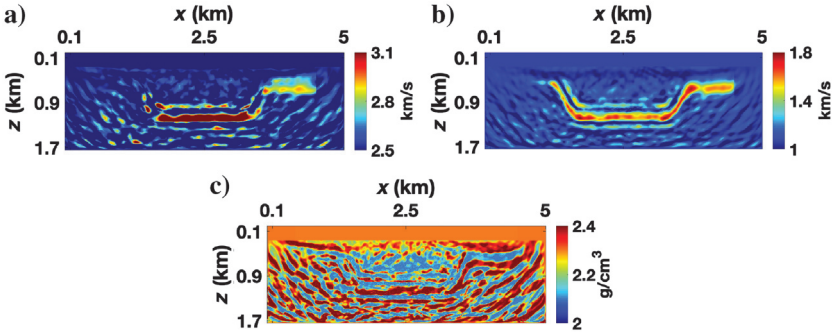

Figure 4. Baseline models estimated by conventional FWI using Wavelet 1: (a) V_{P0}, (b) V_{S0}, and (c) ρ.

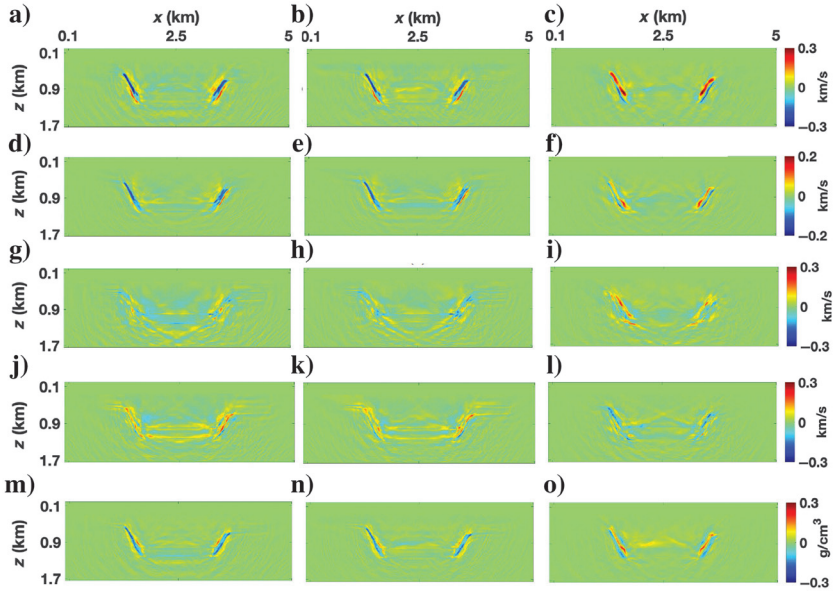

Figure 5. Time-lapse parameter variations reconstructed by the source-independent algorithm with Wavelet 1. The parallel-difference method: (a) V_{P0}, (d) V_{S0}, (g) $V_{\mathrm{hor,P}}$, (j) $V_{\mathrm{nmo,P}}$, and (m) ρ. The sequential-difference method: (b) V_{P0}, (e) V_{S0}, (h) $V_{\mathrm{hor,P}}$, (k) $V_{\mathrm{nmo,P}}$, and (n) ρ. The double-difference method: (c) V_{P0}, (f) V_{S0}, (i) $V_{\mathrm{hor,P}}$, (l) $V_{\mathrm{nmo,P}}$, and (o) ρ.

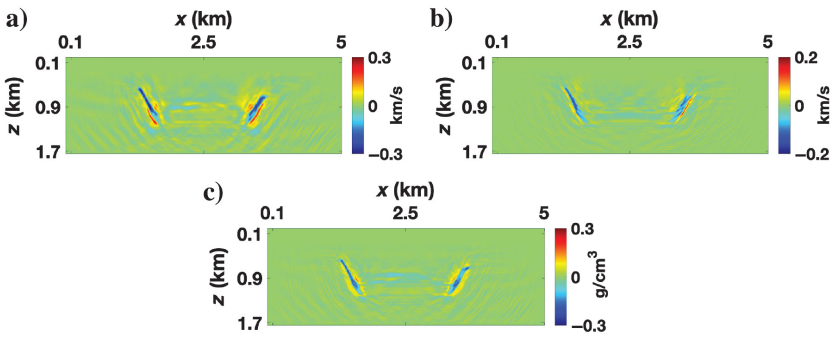

Figure 6. Time-lapse parameter variations estimated by the source-independent algorithm with the spike wavelet (Wavelet 2) using the parallel-difference method: (a) V_{P0}, (b) V_{S0}, and (c) ρ.

Downloaded 03/10/22 to 138.67.12.93. Redistribution subject to SEG license or copyright; see Terms of Use at http://library.seg.org/page/policies/terms
DOI:10.1190/geo2021-0306.1

correct central frequency (the same as for the actual wavelet) to simulate the baseline seismogram and generate the "composite" data. The monitor inversion is still performed using the source-independent algorithm with Wavelet 1. In this case, the reconstructed parameter variations in the target area have the correct sign (Figure 7b) and are sufficiently close to the benchmark results. Evidently, the double-difference method has to be applied with a wavelet that has a sufficiently accurate frequency to properly estimate the temporal parameter variations. If the data for the inverted baseline model are simulated using the actual wavelet (FWI is still performed with Wavelet 1), the double-difference method (Figure 7c) produces the time-lapse changes in the velocity V_{P0} with higher resolution than the other two methods (Figure 5a and 5b).

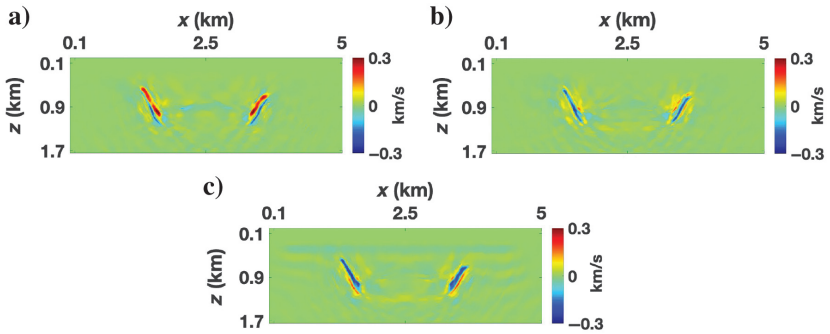

Figure 7. Time-lapse variations of the velocity V_{P0} reconstructed by the source-independent algorithm using the double-difference method. FWI is performed with Wavelet 1, whereas the data for the inverted baseline model ($\mathbf{d}_b^{sim}$) are generated with: (a) Wavelet 1, (b) a signal that has the shape of Wavelet 1 but correct frequency, (c) the actual wavelet.

One possible solution to at least partially resolve the issue with errors in the simulated baseline data generated with a distorted wavelet is to apply dynamic seismic warping. This method has been proposed for time-shift estimation in time-lapse processing by matching traces from the baseline and monitor surveys using the criterion of minimal dissimilarity (Rickett et al., 2007; Hale, 2013; Holschuh et al., 2014; Venstad, 2014; Li et al., 2019). We will explore this method as part of our future research in anisotropic time-lapse FWI.

Influence of noise

Next, the data are contaminated with Gaussian noise that has the signal-to-noise ratio equal to 16, a realistic value for field data. We employ just the parallel-difference method due to its general robustness for noisy data (Liu and Tsvankin, 2021). Here we show only the parameters V_{P0}, V_{S0}, and ρ reconstructed by conventional FWI using the actual source wavelet (benchmark results) and by the source-independent algorithm.

The baseline models (especially V_{P0}) inverted by the source-independent algorithm using Wavelet 1 are somewhat distorted, likely due to the noise amplification in the convolution and cross-correlation operations. However, the source-independent algorithm (Figure 8d and 8e) surprisingly produces a slightly more accurate reconstruction of the baseline velocities in the "reservoir" compared to conventional FWI applied with the actual wavelet (Figure 8a and 8b). Still, the time-lapse variations of V_{P0} estimated by our algorithm (Figure 8j) have

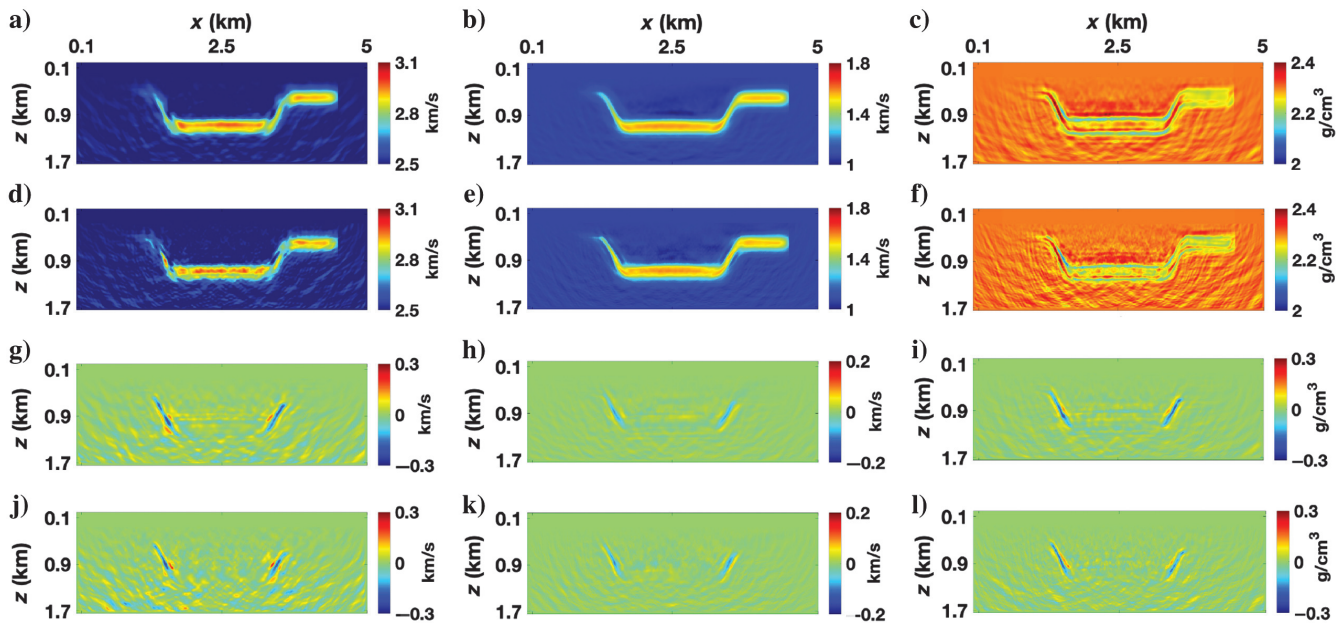

Figure 8. Inverted baseline models and time-lapse variations obtained from noisy data (signal-to-noise ratio is 16). The baseline models obtained by conventional FWI with the actual wavelet [(a) V_{P0}, (b) V_{S0}, (c) ρ] and by the source-independent FWI with Wavelet 1 [(d) V_{P0}, (e) V_{S0}, (f) ρ]. The time-lapse variations obtained by conventional FWI with the actual wavelet [(g) V_{P0}, (h) V_{S0}, (i) ρ] and by the source-independent FWI with Wavelet 1 [(j) V_{P0}, (k) V_{S0}, (l) ρ].

Downloaded 03/10/22 to 138.67.12.93. Redistribution subject to SEG license or copyright; see Terms of Use at http://library.seg.org/page/policies/terms
DOI:10.1190/geo2021-0306.1

a somewhat lower resolution than the benchmark section (Figure 8g). Nevertheless, the changes in the velocity V_{S0} reconstructed by the source-independent FWI (Figure 8k) are close to those obtained with the actual wavelet (Figure 8h). There is no significant difference between the accuracy of the time-lapse results produced with Wavelet 1 and the spike wavelet (Wavelet 2; not shown). This test indicates that our algorithm not only can handle significant wavelet distortions, but also reconstruct the temporal parameter variations for data contaminated with substantial noise.

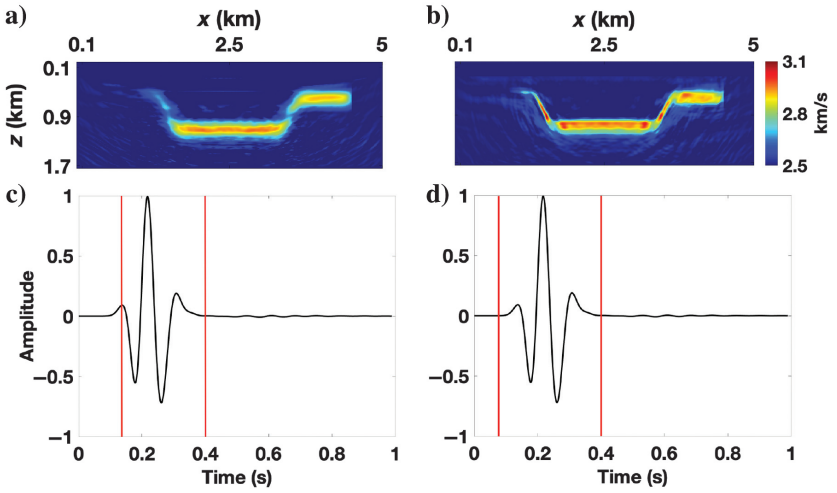

Figure 9. Velocity V_{P0} estimated by the source-independent algorithm from the baseline data for the graben model using the spike wavelet (Wavelet 2) and two time windows: (a) window 1 (plot [c]) and (b) window 2 (plot [d]).

Influence of the reference trace and time window

The objective function for the source-independent FWI (equation 2) is sensitive to the choice of the reference trace and time window. Our results show that employing a reference trace that represents the average of several near-offset traces produces smaller errors compared to using the zero-offset trace; the worst results are obtained using a far-offset trace. This is not surprising because of the higher data fidelity close to the source (Xu et al., 2006; Choi and Alkhalifah, 2011; Zhang et al., 2016). An arrival-time (normal-moveout) correction needs to be applied to the near-offset traces to ensure their in-phase stacking in generating the averaged reference trace. Although NMO stretch can lead to a loss of resolution, it is usually negligible for small offset-to-depth ratios.

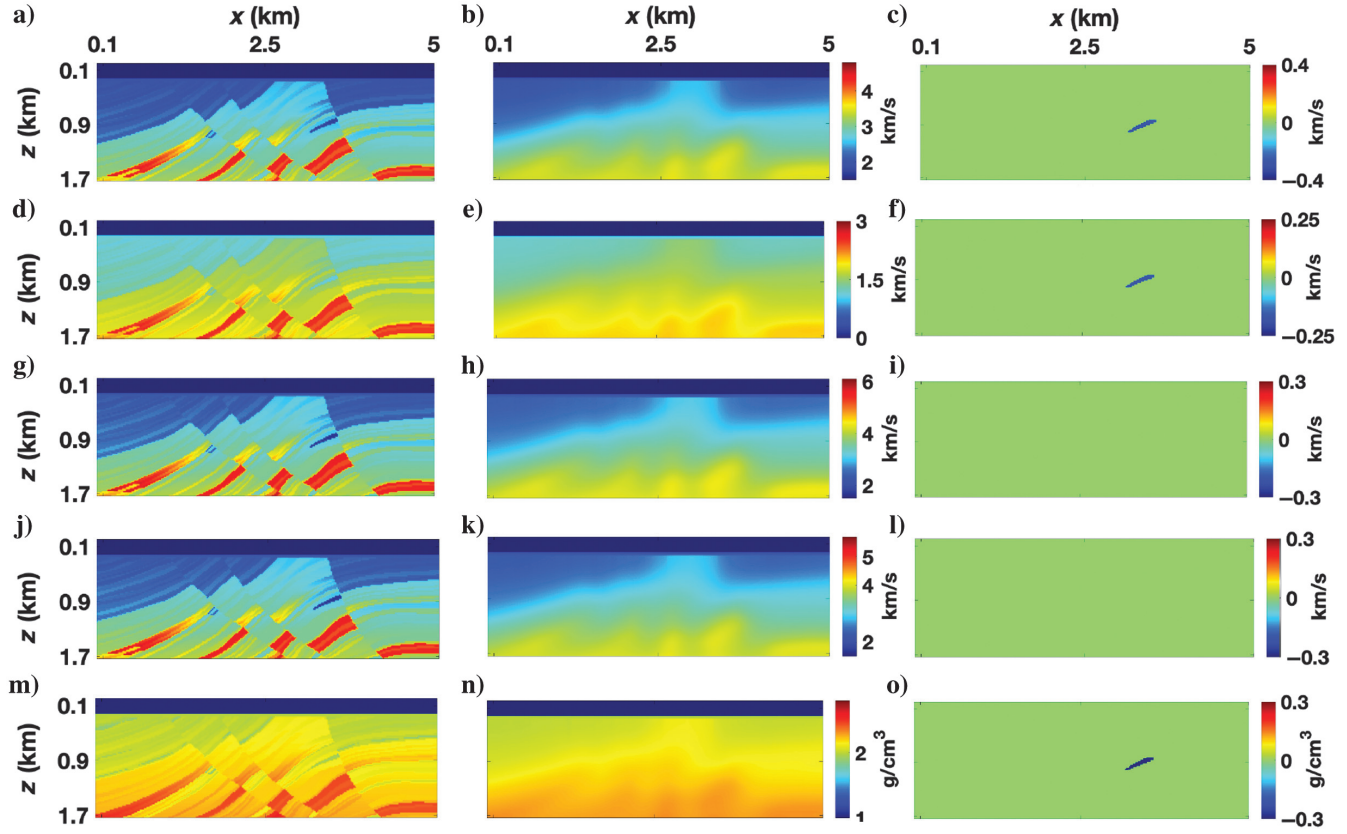

Figure 10. Baseline parameters of the modified VTI Marmousi model with a grid size of 10 × 10 m: (a) V_{P0}, (d) V_{S0}, (g) $V_{hor,P}$, (j) $V_{nmo,P}$, and (m) ρ. The initial baseline model of: (b) V_{P0}, (e) V_{S0}, (h) $V_{hor,P}$, (k) $V_{nmo,P}$, and (n) ρ. The actual time-lapse differences for (c) V_{P0}, (f) V_{S0}, (i) $V_{hor,P}$, (l) $V_{nmo,P}$, and (o) ρ.

Downloaded 03/10/22 to 138.67.12.93. Redistribution subject to SEG license or copyright; see Terms of Use at http://library.seg.org/page/policies/terms
DOI:10.1190/geo2021-0306.1

As mentioned previously, time windowing mitigates the artifacts (noise) caused by the convolution and cross-correlation operations. However, the reference trace may not contain enough information about the source signal if the window is too narrow. Figure 9 shows the velocity V_{P0} reconstructed from the baseline data for the graben model. The source-independent FWI is applied with the spike wavelet and two different time windows. If the window does not capture the entire first arrival (Figure 9c), the graben structure is poorly resolved because the reference trace does not provide sufficient information about the wavelet (Figure 9a). The section in Figure 9b is reconstructed with higher resolution because the time window is closer to optimal, as it includes the first arrival (Figure 9d). This observation agrees with the conclusions of Zhang et al. (2016). Therefore, the time window in our tests is chosen to contain the full waveform of the first arrival (such as the direct P-wave).

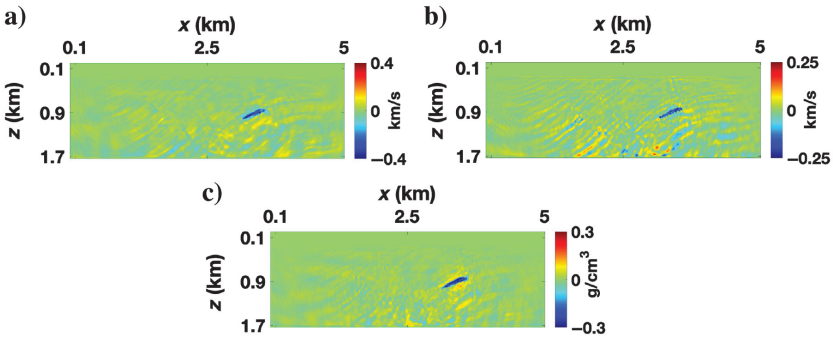

Figure 11. Time-lapse variations for the Marmousi model obtained by conventional FWI using the parallel-difference method with the actual wavelet (benchmark results): (a) V_{P0}, (b) V_{S0}, and (c) ρ.

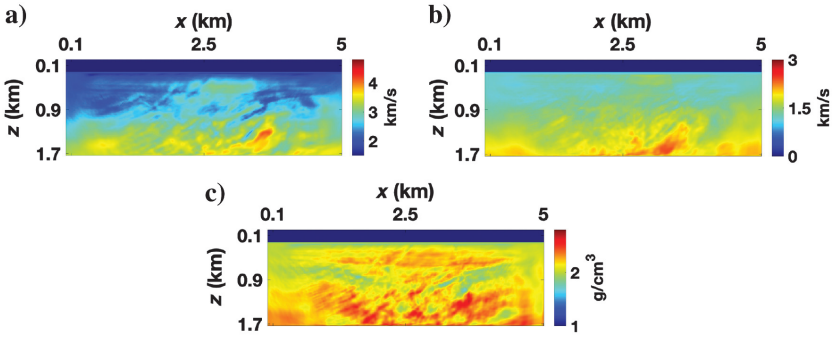

Figure 12. Baseline Marmousi models produced by conventional FWI using a wavelet with only a shape distortion: (a) V_{P0}, (b) V_{S0}, and (c) ρ.

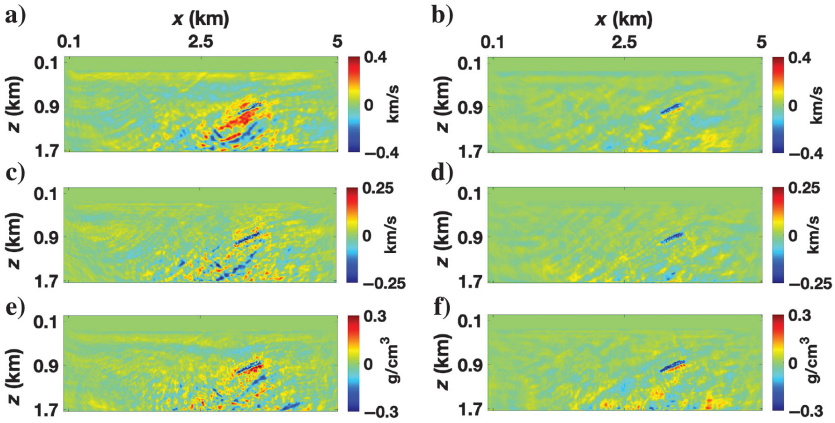

Figure 13. Time-lapse parameter variations for the Marmousi model obtained by the source-independent algorithm with Wavelet 1. The parallel-difference method: (a) V_{P0}, (c) V_{S0}, and (e) ρ. The sequential-difference method: (b) V_{P0}, (d) V_{S0}, and (f) ρ.

VTI Marmousi model

Next, we apply our algorithm to the modified VTI Marmousi model (Figure 10), with data simulated using OBC-style acquisition. The source/receiver geometry is the same as that for the graben model but the receivers are at a depth of 230 m, which corresponds to the water bottom. The time-lapse parameters for the monitor survey are obtained by reducing the baseline vertical velocities V_{P0}, V_{S0} and density ρ in the target area (between the depths of 870 m and 1100 m) by 15% (Figure 10c, 10f, and 10o). The reference trace used in the source-independent algorithm is recorded 70 m away from the source.

As before, elastic FWI is applied to the vertical and horizontal particle-velocity components. After generating the observed data, the benchmark parameter changes are obtained by the conventional FWI algorithm using the parallel-difference method with the actual wavelet (Figure 11). Despite the model complexity and small thickness of the "reservoir," the time-lapse variations are reconstructed with sufficiently high resolution.

Next, we perform conventional FWI of the baseline data using Wavelet 1. However, the inversion becomes unstable and does not converge, likely due to the increased sensitivity to wavelet distortions for this structurally complex model. Then we employ a wavelet with the same shape distortion as Wavelet 1 but correct central frequency. Still, the geologic structure is not properly resolved in the inverted baseline models (Figure 12), and it is obvious that conventional FWI is incapable of reconstructing the time-lapse changes with the inaccurate wavelet.

Because of the problems with the double-difference method discussed previously, the source-independent algorithm is applied only with the other two strategies using the same distorted wavelet (Wavelet 1). In contrast to the graben model, the sequential-difference method (Figure 13b, 13d, and 13f) reconstructs the temporal variations with higher resolution and fewer artifacts than the parallel-difference method (Figure 13a, 13c, and 13e).

Clearly, the performance of these methods varies with the model complexity. Because FWI is implemented using a local optimization technique, the updating algorithm generally converges toward the minimum of the objective function closest to the initial model. The convolution operations in the

Downloaded 03/10/22 to 138.67.12.93. Redistribution subject to SEG license or copyright; see Terms of Use at http://library.seg.org/page/policies/terms
DOI:10.1190/geo2021-0306.1

source-independent method make the shape of the objective function more complex, and the pronounced heterogeneity of the Marmousi model increases the inversion nonlinearity. Starting with the inverted baseline model (which is relatively close to the monitor model) in the sequential-difference method improves the convergence toward the monitor model, which yields more accurate time-lapse variations (Figure 13b, 13d, and 13f).

Comparison of the output of the source-independent FWI applied with the sequential-difference method (Figure 13b, 13d, and 13f) and the benchmark results (Figure 11) shows that despite the combination of the significantly distorted wavelet and pronounced heterogeneity, our algorithm reconstructs the time-lapse variations with acceptable resolution. The somewhat lower accuracy of the source-independent technique (as well as additional artifacts) for the Marmousi model as compared to the graben structure is likely due to the increased medium complexity. In particular, multiple reflections, which could be captured by the time window used in the convolution operations, may hinder the convergence of the algorithm.

CONCLUSIONS

We implemented a "source-independent" time-lapse FWI algorithm for VTI media in the time domain. The modified FWI objective function is designed to mitigate the dependence of the inverted parameters on the accuracy of the source wavelet by employing two additional data sets obtained by convolution operations. The reference traces used in the convolutions should be recorded near the source to ensure high fidelity of the source signature. The convolution time window is chosen to include the entire first arrival (e.g., the direct P-wave), so that the reference trace contains sufficient source information.

The synthetic examples demonstrate that the developed source-independent algorithm can accurately reconstruct the time-lapse variations even for significantly distorted source signals (such as the spike wavelet). The testing also confirms the ability of the method to deal with noisy data and strongly heterogeneous media, although the results for the Marmousi model are somewhat inferior to those for the simpler graben structure. The source-independent technique is particularly important in time-lapse processing because it can handle the non-repeatability of the source wavelet.

ACKNOWLEDGMENTS

We thank the members of the Anisotropy-Team at the Center for Wave Phenomena (CWP) at Colorado School of Mines for useful discussions. This work is supported by the Consortium Project on Seismic Inverse Methods for Complex Structures at CWP.

DATA AND MATERIALS AVAILABILITY

Data associated with this research are available and can be obtained by contacting the corresponding author.

APPENDIX A

INVERSION GRADIENTS FOR THE SOURCE-INDEPENDENT FWI

Starting with Choi and Alkhalifah (2011), several publications discuss the "source-independent" FWI in the time domain, but none of these papers (e.g., Zhang et al., 2016; Bai and Tsvankin, 2019) presents explicit expressions for the inversion gradients. Following Kamath and Tsvankin (2016), we give an explicit derivation of the gradient of the source-independent FWI with respect to the VTI parameters. Note that the objective function and the generation of the back-propagated wavefield here are more complex than in conventional FWI.

To minimize the objective function (equation 2), the simulated wavefield $\mathbf{d}^{\mathrm{sim}}(\mathbf{x}_r, t)$ is generated using the wave equation for arbitrarily anisotropic, heterogeneous media:

$$\rho \frac{\partial^2 d_i^{\mathrm{sim}}}{\partial t^2} - \frac{\partial}{\partial x_j}\left(c_{ijkl}\frac{\partial d_k^{\mathrm{sim}}}{\partial x_l}\right) = f_i, \tag{A-1}$$

where $\mathbf{d}$ is the displacement field, ρ is the density, $\mathbf{f}$ is the density of the body forces, and c_{ijkl} $(i, j, k, l = 1, 2, 3)$ are the stiffness coefficients.

The initial conditions for the displacement are:

$$\mathbf{d}^{\mathrm{sim}}(\mathbf{x}, 0) = 0, \quad \frac{\partial \mathbf{d}^{\mathrm{sim}}(\mathbf{x}, 0)}{\partial t} = 0, \tag{A-2}$$

and the radiation boundary condition,

$$\mathbf{d}^{\mathrm{sim}}(\mathbf{x}, t)|_{\mathbf{x}\to\infty} \to 0. \tag{A-3}$$

Adopting the Lagrange multiplier method, we can define the Lagrangian Δ as:

$$\begin{aligned}\Delta = &\frac{1}{2}\sum_r \int_0^T ||\mathbf{d}^{\mathrm{sim}}(\mathbf{x},t) * W\mathbf{d}_{\mathrm{ref}}^{\mathrm{obs}}(\mathbf{x_f},t) - \mathbf{d}^{\mathrm{obs}}(\mathbf{x},t) * W d_{\mathrm{ref}}^{\mathrm{sim}}(\mathbf{x_f},t)||^2 dt \\ &- \int_0^T \int_\Omega \lambda_i \left[\rho \frac{\partial^2 d_i^{\mathrm{sim}}}{\partial t^2} - \frac{\partial}{\partial x_j}\left(c_{ijkl}\frac{\partial u_k}{\partial x_l}\right) - f_i\right] dV dt,\end{aligned} \tag{A-4}$$

where Ω is the integration domain (volume V), and $\boldsymbol{\lambda}(\mathbf{x}, t)$ is the yet unknown Lagrangian multiplier. After intergration by parts and application of the Gaussian divergence theorem, the change in the Lagrangian can be found in the following form:

$$\begin{aligned}\delta\Delta = &-\int_0^T \sum_{r=1}^N [d_i^{\mathrm{sim}}(\mathbf{x},t) * d_{\mathrm{ref}}^{\mathrm{obs}}(\mathbf{x_f},t) - d_i^{\mathrm{obs}}(\mathbf{x},t) * d_{\mathrm{ref}}^{\mathrm{sim}}(\mathbf{x_f},t)] \\ &\times d_i^{\mathrm{obs}}(\mathbf{x},t)\delta(\mathbf{x}-\mathbf{x}_r)\delta d_{\mathrm{ref}}^{\mathrm{sim}}(\mathbf{x_f},t)dt \\ &\int_0^T \int_\Omega \sum_{r=1}^N [d_i^{\mathrm{sim}}(\mathbf{x},t) * d_{\mathrm{ref}}^{\mathrm{obs}}(\mathbf{x_f},t) - d_i^{\mathrm{obs}}(\mathbf{x},t) * d_{\mathrm{ref}}^{\mathrm{sim}}(\mathbf{x_f},t)] \\ &\times d_{\mathrm{ref}}^{\mathrm{obs}}(\mathbf{x_f},t)\delta(\mathbf{x}-\mathbf{x}_r)\delta d_i^{\mathrm{sim}}(\mathbf{x},t)dV dt \\ &- \int_0^T \int_\Omega \delta c_{ijkl}\frac{\partial d_k^{\mathrm{sim}}}{\partial x_l}\frac{\partial \lambda_i}{\partial x_j} dV dt \\ &- \int_0^T \int_\Omega \left[\rho\frac{\partial^2 \lambda_i}{\partial t^2} - \frac{\partial}{\partial x_j}\left(c_{ijkl}\frac{\partial \lambda_k}{\partial x_l}\right)\right]\delta d_i^{\mathrm{sim}} dV dt \\ &- \int_\Omega \left[\rho\lambda_i \frac{\partial(\delta d_i^{\mathrm{sim}})}{\partial t} - \rho\delta d_i^{\mathrm{sim}}\frac{\partial \lambda_i}{\partial t}\right]\Big|_0^T dV \\ &+ \int_0^T \int_{\partial\Omega} \lambda_i \left[\delta c_{ijkl}\frac{\partial d_k^{\mathrm{sim}}}{\partial x_l} + c_{ijkl}\frac{\partial(\delta d_k^{\mathrm{sim}})}{\partial x_l}\right] n_j dS dt \\ &- \int_0^T \int_{\partial\Omega} \delta d_i^{\mathrm{sim}} c_{ijkl}\frac{\partial \lambda_k}{\partial x_l} n_j dS dt,\end{aligned} \tag{A-5}$$

Downloaded 03/10/22 to 138.67.12.93. Redistribution subject to SEG license or copyright; see Terms of Use at http://library.seg.org/page/policies/terms
DOI:10.1190/geo2021-0306.1

where $\partial\Omega$ is the surface of Ω, $\mathbf{n}$ is the vector normal to $\partial\Omega$, and $r = 1, 2, 3 \ldots N$ denotes the receivers (Kamath and Tsvankin, 2016). Following Choi and Alkhalifah (2011), the second term of equation A-5 can be ignored because it operates with only the reference trace. The initial and boundary conditions for the perturbation in $\mathbf{d}^{\mathrm{sim}}(\mathbf{x}, t)$ are given by:

$$\delta\mathbf{d}^{\mathrm{sim}}(\mathbf{x},0) = 0, \quad \frac{\partial[\delta\mathbf{d}^{\mathrm{sim}}(\mathbf{x},0)]}{\partial t} = 0, \quad \delta\mathbf{d}^{\mathrm{sim}}(\mathbf{x},t)|_{\mathbf{x}\to\infty} \to 0. \tag{A-6}$$

Assuming that there are no parameter perturbations, the wavefield $\boldsymbol{\lambda}$ at time T is subject to the following conditions:

$$\boldsymbol{\lambda}(\mathbf{x}, T) = 0, \quad \frac{\partial\boldsymbol{\lambda}(\mathbf{x}, T)}{\partial t} = 0, \tag{A-7}$$

and the radiation boundary condition,

$$\boldsymbol{\lambda}(\mathbf{x}, t)|_{\mathbf{x}\to\infty} \to 0. \tag{A-8}$$

Using equations A-7 and A-8, equation A-5 can be reduced to:

$$\begin{aligned}\delta\Delta = &\int_0^T \int_\Omega \sum_{r=1}^{N} [d_i^{\mathrm{sim}}(\mathbf{x}, t) * d_{\mathrm{ref}}^{\mathrm{obs}}(\mathbf{x_f}, t) - d_i^{\mathrm{obs}}(\mathbf{x}, t) * d_{\mathrm{ref}}^{\mathrm{sim}}(\mathbf{x_f}, t)] \\ &\times d^{\mathrm{obs}}(\mathbf{x_f}, t)\delta(\mathbf{x} - \mathbf{x}_r)\delta d_i^{\mathrm{sim}} dV dt \\ &- \int_0^T \int_\Omega \delta c_{ijkl} \frac{\partial d_k^{\mathrm{sim}}}{\partial x_l} \frac{\partial \lambda_i}{\partial x_j} dV dt \\ &- \int_0^T \int_\Omega \left[\rho \frac{\partial^2 \lambda_i}{\partial t^2} - \frac{\partial}{\partial x_j}\left(c_{ijkl}\frac{\partial \lambda_k}{\partial x_l}\right)\right] \delta d_i^{\mathrm{sim}} dV dt.\end{aligned} \tag{A-9}$$

According to Plessix (2006), the condition $(\partial\Delta/\partial\boldsymbol{\lambda}) = 0$ leads to the so-called "state equations." The adjoint state equations are obtained by setting $(\partial\Delta/\partial\mathbf{d}^{\mathrm{sim}}) = 0$. Taking the derivative of equation A-9 leads to the adjoint state equation,

$$\begin{aligned}\rho \frac{\partial^2 \lambda_i}{\partial t^2} - \frac{\partial}{\partial x_j}\left(c_{ijkl}\frac{\partial \lambda_k}{\partial x_l}\right) &= \sum_{r=1}^{N} \{[d_i^{\mathrm{sim}}(\mathbf{x}_r, t) * d_{\mathrm{ref}}^{\mathrm{obs}}(\mathbf{x_f}, t) \\ &- d_i^{\mathrm{obs}}(\mathbf{x}_r, t) * d_{\mathrm{ref}}^{\mathrm{sim}}(\mathbf{x_f}, t)] d^{\mathrm{obs}}(\mathbf{x_f}, t)\} \\ &= \sum_{r=1}^{N} \{d_{\mathrm{ref}}^{\mathrm{obs}}(\mathbf{x_f}, t) \otimes [d_i^{\mathrm{sim}}(\mathbf{x}_r, t) * d_{\mathrm{ref}}^{\mathrm{obs}}(\mathbf{x_f}, t) \\ &- d_i^{\mathrm{obs}}(\mathbf{x}_r, t) * d_{\mathrm{ref}}^{\mathrm{sim}}(\mathbf{x_f}, t)]\},\end{aligned} \tag{A-10}$$

where $\otimes$ denotes cross-correlation. Because $\mathbf{d}^{\mathrm{sim}}$ satisfies the wave equation, Δ is equal to the objective function S_{b} from equation 2 (see equation A-4) (Plessix, 2006). Hence, the change δS_{b} due to the perturbations of the stiffness coefficients is given by:

$$\delta S_{\mathrm{b}} = -\int_0^T \int_\Omega \delta c_{ijkl} \frac{\partial d_i^{\mathrm{sim}}}{\partial x_j} \frac{\partial \lambda_k}{\partial u_l} dV dt. \tag{A-11}$$

To simulate the Lagrangian multiplier, we follow Liu and Tromp (2006) in defining the "adjoint wavefield" $\boldsymbol{\psi}$:

$$\boldsymbol{\psi}(\mathbf{x}, t) \equiv \boldsymbol{\lambda}(\mathbf{x}, T - t). \tag{A-12}$$

The adjoint wavefield $\boldsymbol{\psi}$ satisfies the following wave equation with a reversed-time source function:

$$\begin{aligned}&\rho \frac{\partial^2 \psi_i}{\partial t^2} - \frac{\partial}{\partial x_j}\left(c_{ijkl}\frac{\partial \psi_k}{\partial x_l}\right) = \\ &\sum_{r=1}^{N} \{d^{\mathrm{obs}}(\mathbf{x_f}, T - t) \otimes [d_i^{\mathrm{sim}}(\mathbf{x}_r, T - t) * d_{\mathrm{ref}}^{\mathrm{obs}}(\mathbf{x_f}, T - t) \\ &- d_i^{\mathrm{obs}}(\mathbf{x}_r, T - t) * d_{\mathrm{ref}}^{\mathrm{sim}}(\mathbf{x_f}, T - t)]\}.\end{aligned} \tag{A-13}$$

The initial conditions for $\boldsymbol{\psi}$ are

$$\boldsymbol{\psi}(\mathbf{x}, 0) = 0, \quad \frac{\partial\boldsymbol{\psi}(\mathbf{x}, 0)}{\partial t} = 0, \tag{A-14}$$

and the boundary condition is

$$\boldsymbol{\psi}(\mathbf{x}, t)|_{\mathbf{x}\to\infty} \to 0. \tag{A-15}$$

From equations A-10 and A-11, we can derive the inversion gradient with respect to the stiffness coefficients (Kamath and Tsvankin, 2016):

$$\frac{\partial S}{\partial c_{ijkl}} = -\int_0^T \frac{\partial d_i^{\mathrm{sim}}}{\partial x_j} \frac{\partial \psi_k}{\partial x_l} dt. \tag{A-16}$$

The gradient of S with respect to the chosen parameters m_n can be obtained using the chain rule:

$$\frac{\partial S}{\partial m_n} = \sum_{ijkl} \frac{\partial S}{\partial c_{ijkl}} \frac{\partial c_{ijkl}}{\partial m_n}. \tag{A-17}$$

For VTI media, we define $m_1 = V_{\mathrm{P0}}, m_2 = V_{\mathrm{S0}}, m_3 = V_{\mathrm{nmo,P}}, m_4 = V_{\mathrm{hor,P}}, m_5 = V_{\mathrm{hor,SH}} = V_{\mathrm{S0}}\sqrt{1+2\gamma}$, and $m_6 = \rho$ (Singh et al., 2020). The stiffness elements can be expressed using the velocities as follows (e.g., Tsvankin, 2012; Kamath and Tsvankin, 2016):

Downloaded 03/10/22 to 138.67.12.93. Redistribution subject to SEG license or copyright; see Terms of Use at http://library.seg.org/page/policies/terms
DOI:10.1190/geo2021-0306.1

$$\begin{aligned}
C_{11} &= \rho V_{\mathrm{hor,P}}^2,\\
C_{13} &= \rho\left[\sqrt{(V_{\mathrm{P0}}^2 - V_{\mathrm{S0}}^2)(V_{\mathrm{nmo,P}}^2 - V_{\mathrm{S0}}^2)} - V_{\mathrm{S0}}^2\right],\\
C_{33} &= \rho V_{\mathrm{P0}}^2,\\
C_{55} &= \rho V_{\mathrm{S0}}^2,\\
C_{66} &= \rho V_{\mathrm{hor,SH}}^2.
\end{aligned} \tag{A-18}$$

Note that C_{66} is not estimated in our synthetic examples because the modeling algorithm simulates only P- and SV-waves, which are polarized in the vertical propagation plane. Equations A-17 and A-18 allow us to obtain the gradient with respect to the model parameters:

$$\frac{\partial S}{\partial V_{\mathrm{P0}}} = -2\rho V_{\mathrm{P0}} \int_0^T \left[\frac{\partial \psi_x}{\partial z}\frac{\partial d_z^{\mathrm{sim}}}{\partial z} + \frac{q}{2}\left(\frac{\partial \psi_x}{\partial z}\frac{\partial d_z^{\mathrm{sim}}}{\partial z} + \frac{\partial \psi_z}{\partial z}\frac{\partial d_x^{\mathrm{sim}}}{\partial x} + \frac{\partial \psi_y}{\partial y}\frac{\partial d_z^{\mathrm{sim}}}{\partial z} + \frac{\partial \psi_z}{\partial z}\frac{\partial d_y^{\mathrm{sim}}}{\partial y}\right)\right] dt, \tag{A-19}$$

$$\begin{aligned}
\frac{\partial S}{\partial V_{\mathrm{S0}}} = {}& 2\rho V_{\mathrm{S0}} \int_0^T \left[\left(1 + \frac{q}{2} + \frac{1}{2q}\right)\left(\frac{\partial \psi_x}{\partial x}\frac{\partial d_z^{\mathrm{sim}}}{\partial z} + \frac{\partial \psi_z}{\partial z}\frac{\partial d_x^{\mathrm{sim}}}{\partial x} + \frac{\partial \psi_y}{\partial y}\frac{\partial d_z^{\mathrm{sim}}}{\partial z} + \frac{\partial \psi_z}{\partial z}\frac{\partial d_y^{\mathrm{sim}}}{\partial y}\right)\right.\\
&\left. - \left(\frac{\partial \psi_x}{\partial z} + \frac{\partial \psi_z}{\partial x}\right)\left(\frac{\partial d_x^{\mathrm{sim}}}{\partial z} + \frac{\partial d_z^{\mathrm{sim}}}{\partial x}\right) - \left(\frac{\partial \psi_y}{\partial z} + \frac{\partial \psi_z}{\partial y}\right)\left(\frac{\partial d_y^{\mathrm{sim}}}{\partial z} + \frac{\partial d_z^{\mathrm{sim}}}{\partial y}\right)\right] dt,
\end{aligned} \tag{A-20}$$

$$\frac{\partial S}{\partial V_{\mathrm{nmo,P}}} = -\frac{\rho V_{\mathrm{nmo,P}}}{q} \int_0^T \left(\frac{\partial \psi_x}{\partial x}\frac{\partial d_z^{\mathrm{sim}}}{\partial z} + \frac{\partial \psi_z}{\partial z}\frac{\partial d_x^{\mathrm{sim}}}{\partial x} + \frac{\partial \psi_y}{\partial y}\frac{\partial d_z^{\mathrm{sim}}}{\partial z}\right) dt, \tag{A-21}$$

$$\frac{\partial S}{\partial V_{\mathrm{hor,P}}} = -2\rho V_{\mathrm{hor,P}} \int_0^T \left(\frac{\partial \psi_y}{\partial y} + \frac{\partial \psi_x}{\partial x}\right)\left(\frac{\partial d_y^{\mathrm{sim}}}{\partial y} + \frac{\partial d_x^{\mathrm{sim}}}{\partial x}\right) dt, \tag{A-22}$$

$$\begin{aligned}
\frac{\partial S}{\partial V_{\mathrm{hor,SH}}} = {}& -2\rho V_{\mathrm{hor,S}} \int_0^T \left[\left(\frac{\partial \psi_x}{\partial y} + \frac{\partial \psi_y}{\partial x}\right)\left(\frac{\partial d_x^{\mathrm{sim}}}{\partial y} + \frac{\partial d_y^{\mathrm{sim}}}{\partial x}\right)\right.\\
&\left. - 2\left(\frac{\partial \psi_y}{\partial y}\frac{\partial d_x^{\mathrm{sim}}}{\partial x} + \frac{\partial \psi_x}{\partial x}\frac{\partial d_y^{\mathrm{sim}}}{\partial y}\right)\right] dt,
\end{aligned} \tag{A-23}$$

$$\begin{aligned}
\frac{\partial S}{\partial \rho} = {}& -\int_0^T \left\{V_{\mathrm{P0}}^2\left(\frac{\partial \psi_z}{\partial z}\frac{\partial d_z^{\mathrm{sim}}}{\partial z}\right)\right.\\
&+ V_{\mathrm{hor,P}}^2\left(\frac{\partial \psi_x}{\partial x}\frac{\partial d_x^{\mathrm{sim}}}{\partial x} + \frac{\partial \psi_y}{\partial y}\frac{\partial d_y^{\mathrm{sim}}}{\partial y} + \frac{\partial \psi_x}{\partial x}\frac{\partial d_y^{\mathrm{sim}}}{\partial y} + \frac{\partial \psi_y}{\partial y}\frac{\partial d_x^{\mathrm{sim}}}{\partial x}\right)\\
&+ V_{\mathrm{S0}}^2\left[\left(\frac{\partial \psi_x}{\partial z} + \frac{\partial \psi_z}{\partial x}\right)\left(\frac{\partial d_x^{\mathrm{sim}}}{\partial z} + \frac{\partial d_z^{\mathrm{sim}}}{\partial x}\right) + \left(\frac{\partial \psi_y}{\partial z} + \frac{\partial \psi_z}{\partial y}\right)\left(\frac{\partial d_y^{\mathrm{sim}}}{\partial z} + \frac{\partial d_z^{\mathrm{sim}}}{\partial y}\right)\right]\\
&+ V_{\mathrm{hor,SH}}^2\left[\left(\frac{\partial \psi_x}{\partial y} + \frac{\partial \psi_y}{\partial x}\right)\left(\frac{\partial d_x^{\mathrm{sim}}}{\partial y} + \frac{\partial d_y^{\mathrm{sim}}}{\partial x}\right) - 2\frac{\partial \psi_y}{\partial y}\frac{\partial d_x^{\mathrm{sim}}}{\partial x} - 2\frac{\partial \psi_x}{\partial x}\frac{\partial d_y^{\mathrm{sim}}}{\partial y}\right]\\
&+ \left[\sqrt{(V_{\mathrm{nmo,P}}^2 - V_{\mathrm{S0}}^2)(V_{\mathrm{P0}}^2 - V_{\mathrm{S0}}^2)} - V_{\mathrm{S0}}^2\right]\\
&\times \left[\frac{\partial \psi_z}{\partial z}\frac{\partial d_x^{\mathrm{sim}}}{\partial x} + \frac{\partial \psi_x}{\partial x}\frac{\partial d_z^{\mathrm{sim}}}{\partial z} + \frac{\partial \psi_z}{\partial z}\frac{\partial d_y^{\mathrm{sim}}}{\partial y} + \frac{\partial \psi_y}{\partial y}\frac{\partial d_z^{\mathrm{sim}}}{\partial z}\right]\\
&\left. + v_x \boldsymbol{\psi}_x + v_y \boldsymbol{\psi}_y + v_z \boldsymbol{\psi}_z\right\} dt,
\end{aligned} \tag{A-24}$$

where

$$q = \sqrt{\frac{V_{\mathrm{nmo,P}}^2 - V_{\mathrm{S0}}^2}{V_{\mathrm{P0}}^2 - V_{\mathrm{S0}}^2}}. \tag{A-25}$$

Here, $\boldsymbol{v}$ denotes the forward-propagated velocity field and $\boldsymbol{\psi}$ denotes the back-propagated velocity field (Singh et al., 2020).

REFERENCES

Alkhalifah, T., and R. E. Plessix, 2014, A recipe for practical full-waveform inversion in anisotropic media: An analytical parameter resolution study: Geophysics, **79**, no. 3, R91–R101, doi: 10.1190/geo2013-0366.1.

Asnaashari, A., R. Brossier, S. Garambois, F. Audebert, P. Thore, and J. Virieux, 2012, Time-lapse imaging using regularized FWI: A robustness study: 82nd Annual International Meeting, SEG, Expanded Abstracts, doi: 10.1190/segam2012-0699.1.

Asnaashari, A., R. Brossier, S. Garambois, F. Audebert, P. Thore, and J. Virieux, 2015, Time-lapse seismic imaging using regularized full-waveform inversion with a prior model: Which strategy?: Geophysical Prospecting, **63**, 78–98, doi: 10.1111/1365-2478.12176.

Bai, T., and I. Tsvankin, 2019, Source-independent waveform inversion for attenuation estimation in anisotropic media: Geophysical Prospecting, **67**, 2343–2357, doi: 10.1111/1365-2478.12821.

Choi, Y., and T. Alkhalifah, 2011, Source-independent time-domain waveform inversion using convolved wavefields: Application to the encoded multisource waveform inversion: Geophysics, **76**, no. 5, R125–R134, doi: 10.1190/geo2010-0210.1.

Choi, Y., and D.-J. Min, 2012, Source-independent elastic waveform inversion using a logarithmic wavefield: Journal of Applied Geophysics, **76**, 13–22, doi: 10.1016/j.jappgeo.2011.10.013.

Choi, Y., C. Shin, D. J. Min, and T. Ha, 2005, Efficient calculation of the steepest descent direction for source-independent seismic waveform inversion: An amplitude approach: Journal of Computational Physics, **208**, 455–468, doi: 10.1016/j.jcp.2004.09.019.

Denli, H., and L. Huang, 2009, Double-difference elastic waveform tomography in the time domain: 79th Annual International Meeting, SEG, Expanded Abstracts, 2302–2306, doi: 10.1190/1.3255320.

Hale, D., 2013, Dynamic warping of seismic images: Geophysics, **78**, no. 2, S105–S115, doi: 10.1190/geo2012-0327.1.

Holschuh, N. D., C. Li, M. A. Meadows, and S. Dobbs, 2014, Systems and methods for aligning a monitor seismic survey with a baseline seismic survey: U.S. Patent 14,565,117, 1–16.

Jervis, M., A. Bakulin, and R. Smith, 2018, Making time-lapse seismic work in a complex desert environment for CO_2 EOR monitoring — Design and acquisition: The Leading Edge, **37**, 598–606, doi: 10.1190/tle37080598.1.

Kamath, N., and I. Tsvankin, 2016, Elastic full-waveform inversion for VTI media: Methodology and sensitivity analysis: Geophysics, **81**, no. 2, C53–C68, doi: 10.1190/geo2014-0586.1.

Downloaded 03/10/22 to 138.67.12.93. Redistribution subject to SEG license or copyright; see Terms of Use at http://library.seg.org/page/policies/terms
DOI:10.1190/geo2021-0306.1

Lee, K. H., and H. J. Kim, 2003, Source-independent full-waveform inversion of seismic data: Geophysics, **68**, 2010–2015, doi: 10.1190/1.1635054.

Li, C., M. Meadows, and T. Dygert, 2019, Warping least-squares inversion for 4D velocity change: Gulf of Mexico case study: Interpretation, **7**, no. 2, SB23–SB31, doi: 10.1190/INT-2018-0145.1.

Li, Y., T. Alkhalifah, and Q. Guo, 2021, Target-oriented time-lapse waveform inversion using deep learning-assisted regularization: Geophysics, **86**, no. 4, R485–R495, doi: 10.1190/geo2020-0383.1.

Liu, Q., and J. Tromp, 2006, Finite-frequency kernels based on adjoint methods: Bulletin of the Seismological Society of America, **96**, 2383–2397, doi: 10.1785/0120060041.

Liu, Y., and I. Tsvankin, 2021, Methodology of time-lapse elastic full-waveform inversion for VTI media: Journal of Seismic Exploration, **30**, 257–270.

Lumley, D., 2010, 4D seismic monitoring of sequestration: The Leading Edge, **29**, 150–155, doi: 10.1190/1.3304817.

Luo, C. M., S. X. Wang, and S. Y. Yuan, 2014, Effect of inaccurate wavelet phase on prestack waveform inversion: Journal of Applied Geophysics, **11**, 479–488, doi: 10.1007/s11770-014-0453-1.

Pevzner, R., M. Urosevic, D. Popik, V. Shulakova, K. Tertyshnikov, E. Caspari, J. Correa, T. Dance, A. Kepic, S. Glubokovskikh, S. Ziramov, B. Gurevich, R. Singh, M. Raab, M. Watson, T. Daley, M. Robertson, and B. Freifeld, 2017, 4D surface seismic tracks small supercritical CO_2 injection into the subsurface: CO2CRC Otway Project: International Journal of Greenhouse Gas Control, **63**, 150–157, doi: 10.1016/j.ijggc.2017.05.008.

Plessix, R. E., 2006, A review of the adjoint-state method for computing the gradient of a functional with geophysical applications: Geophysical Journal International, **167**, 495–503, doi: 10.1111/j.1365-246X.2006.02978.x.

Plessix, R.-E., S. Michelet, H. Rynja, H. Kuehl, C. Perkins, J. Maag, and P. Hatchell, 2010, Some 3D applications of full waveform inversion: 72nd Annual International Conference and Exhibition — Workshops and Fieldtrips, EAGE, Extended Abstracts, doi: 10.3997/2214-4609.20149933.

Pratt, R. G., 1999, Seismic waveform inversion in the frequency domain — Part 1: Theory and verification in a physical scale model: Geophysics, **64**, 888–901, doi: 10.1190/1.1444597.

Rickett, J., L. Duranti, T. Hudson, B. Regel, and N. Hodgson, 2007, 4D time strain and the seismic signature of geomechanical compaction at Genesis: The Leading Edge, **26**, 644–647, doi: 10.1190/1.2737103.

Schmidt, M., 2005, Least squares optimization with L1-norm regularization: Technical report.

Seo, T., C. Shin, and D. Min, 2005, Efficient calculation of steepest descent direction of source signature independent waveform inversion of logarithmic wavefield: 75th Annual International Meeting, SEG, Expanded Abstracts, 1838–1841, doi: 10.1190/1.1845176.

Singh, S., I. Tsvankin, and E. Z. Naeini, 2020, Full-waveform inversion with borehole constraints for elastic VTI media: Geophysics, **85**, no. 6, R553–R563, doi: 10.1190/geo2019-0816.1.

Singh, S., I. Tsvankin, and E. Zahibi Naeini, 2018, Bayesian framework for elastic full-waveform inversion with facies information: The Leading Edge, **37**, 924–931, doi: 10.1190/tle37120924.1.

Smith, S. S., and I. Tsvankin, 2013, Sensitivity of compaction-induced multicomponent seismic time shifts to variations in reservoir properties: Geophysics, **78**, no. 5, T151–T163, doi: 10.1190/geo2012-0361.1.

Song, Z., P. R. Williamson, and R. G. Pratt, 1995, Frequency-domain acoustic-wave modeling and inversion of crosshole data — Part 2: Inversion method, synthetic experiments and real-data results: Geophysics, **60**, 796–809, doi: 10.1190/1.1443818.

Tarantola, A., 1984, Linearized inversion of seismic reflection data: Geophysical Prospecting, **32**, 998–1015, doi: 10.1111/j.1365-2478.1984.tb00751.x.

Tsvankin, I., 2012, Seismic signatures and analysis of reflection data in anisotropic media, 3rd ed.: SEG.

Venstad, J. M., 2014, Dynamic time warping — An improved method for 4D and tomography time shift estimation?: Geophysics, **79**, no. 5, R209–R220, doi: 10.1190/geo2013-0239.1.

Vigh, D., K. Jiao, D. Watts, and D. Sun, 2014, Elastic full-waveform inversion application using multicomponent measurements of seismic data collection: Geophysics, **79**, no. 2, R63–R77, doi: 10.1190/geo2013-0055.1.

Waldhauser, F., and W. Ellsworth, 2020, A double-difference earthquake location algorithm: Method and application to the northern Hayward fault, California: Bulletin of the Seismological Society of America, **90**, 1353–1368, doi: 10.1785/0120000006.

Wang, H., and T. Alkhalifah, 2018, Microseismic imaging using a source function independent full waveform inversion method: Geophysical Journal International, **214**, 46–57, doi: 10.1093/gji/ggy121.

Wang, H., Q. Guo, T. Alkhalifah, and Z. Wu, 2020, Regularized elastic passive equivalent source inversion with full-waveform inversion: Application to a field monitoring microseismic data set: Geophysics, **85**, no. 6, KS207–KS219, doi: 10.1190/geo2019-0738.1.

Warner, M., A. Ratcliffe, T. Nangoo, J. Morgan, A. Umpleby, N. Shah, V. Vinje, I. Štekl, L. Guasch, C. Win, G. Conroy, and A. Bertrand, 2013, Anisotropic 3D full-waveform inversion: Geophysics, **78**, no. 2, R59–R80, doi: 10.1190/geo2012-0338.1.

Watanabe, T., S. Shimizu, E. Asakawa, and T. Matsuoka, 2004, Differential waveform tomography for time-lapse crosswell seismic data with application to gas hydrate production monitoring: 74th Annual International Meeting, SEG, Expanded Abstracts, 2323–2326, doi: 10.1190/1.1845221.

Xu, K., S. A. Greenhalgh, and M. Wang, 2006, Comparison of source-independent methods of elastic waveform inversion: Geophysics, **71**, no. 6, R91–R100, doi: 10.1190/1.2356256.

Yuan, F., S. Wang, S. Yuan, J. Wang, J. Li, P. Shi, and Y. Liu, 2014, Influence of inaccurate wavelet amplitude on frequency-domain full waveform inversion: 76th Annual International Conference and Exhibition, EAGE, Extended Abstracts, doi: 10.3997/2214-4609.20140855.

Zhang, Q., H. Zhou, Q. Li, H. Chen, and J. Wang, 2016, Robust source-independent elastic full-waveform inversion in the time domain: Geophysics, **81**, no. 2, R29–R44, doi: 10.1190/geo2015-0073.1.

Zhang, X., and J. Zhang, 2012, Edge preserving regularization for seismic traveltime tomography: 82nd Annual International Meeting, SEG, Expanded Abstracts, doi: 10.1190/segam2012-0571.1.

Zhang, Z., and T. Alkhalifah, 2020, High-resolution reservoir characterization using deep learning-aided elastic full-waveform inversion: The North Sea field data example: Geophysics, **85**, no. 4, WA137–WA146, doi: 10.1190/geo2019-0340.1.

Zhang, Z., T. Alkhalifah, E. Z. Naeini, and B. Sun, 2018, Multiparameter elastic full waveform inversion with facies-based constraints: Geophysical Journal International, **213**, 2112–2127, doi: 10.1093/gji/ggy113.

Zhou, B., and S. A. Greenhalgh, 2003, Crosshole seismic inversion with normalized full-waveform amplitude data: Geophysics, **68**, 1320–1330, doi: 10.1190/1.1598125.

Biographies and photographs of the authors are not available.